

Journal of Biomedical Optics

SPIEDigitalLibrary.org/jbo

Identifying brain neoplasms using dye-enhanced multimodal confocal imaging

Dennis Wirth
Matija Snuderl
Sameer Sheth
Churl-Su Kwon
Matthew P. Frosch
William Curry
Anna N. Yaroslavsky

Identifying brain neoplasms using dye-enhanced multimodal confocal imaging

Dennis Wirth,^a Matija Snuderl,^b Sameer Sheth,^c Churl-Su Kwon,^c Matthew P. Frosch,^b William Curry,^c and Anna N. Yaroslavsky^{a,d}

^aUniversity of Massachusetts, Department of Physics and Applied Physics, One University Avenue Lowell, Massachusetts 01854

^bHarvard Medical School, Massachusetts General Hospital, Department of Pathology, 55 Fruit Street, Warren 225, Boston, Massachusetts 02114

^cHarvard Medical School, Massachusetts General Hospital, Department of Neurosurgery, 55 Fruit Street, Gray 502, Boston, Massachusetts 02114

^dHarvard Medical School, Wellman Center for Photomedicine, Massachusetts General Hospital, 55 Fruit Street, BAR314B, Boston, Massachusetts 02114

Abstract. Brain tumors cause significant morbidity and mortality even when benign. Completeness of resection of brain tumors improves quality of life and survival; however, that is often difficult to accomplish. The goal of this study was to evaluate the feasibility of using multimodal confocal imaging for intraoperative detection of brain neoplasms. We have imaged different types of benign and malignant, primary and metastatic brain tumors. We correlated optical images with histopathology and evaluated the possibility of interpreting confocal images in a manner similar to pathology. Surgical specimens were briefly stained in 0.05 mg/ml aqueous solution of methylene blue (MB) and imaged using a multimodal confocal microscope. Reflectance and fluorescence signals of MB were excited at 642 nm. Fluorescence emission of MB was registered between 670 and 710 nm. After imaging, tissues were processed for hematoxylin and eosin (H&E) histopathology. The results of comparison demonstrate good correlation between fluorescence images and histopathology. Reflectance images provide information about morphology and vascularity of the specimens, complementary to that provided by fluorescence images. Multimodal confocal imaging has the potential to aid in the intraoperative detection of microscopic deposits of brain neoplasms. The application of this technique may improve completeness of resection and increase patient survival. © 2012 Society of Photo-Optical Instrumentation Engineers (SPIE). [DOI: 10.1117/1.JBO.17.2.026012]

Keywords: brain cancers; multimodal confocal; fluorescence; reflectance.

Paper 11554 received Sep. 28, 2011; revised manuscript received Dec. 1, 2011; accepted for publication Dec. 22, 2011; published online Feb. 24, 2012.

1 Introduction

Neoplasms of the brain represent a challenge for neurosurgeons, neuropathologists, and oncologists alike. Even low-grade tumors often progress due to inability to achieve complete resection. High-grade tumors almost invariably progress despite multimodality therapy. Mounting evidence suggests that more extensive surgical resection is associated with longer life expectancy for both low- and high-grade gliomas.¹ Therefore, intraoperative diagnosis plays an important role in clinical decisions during the surgery. Optical techniques are capable of providing rapid intraoperative assessment of both excised tissue and the surgical bed.²⁻⁵ As intrinsic contrast of brain neoplasms is often subtle, adjunctive fluorescent contrast agents may be employed. For example, several studies have shown that 5-aminolevulinic acid (ALA) induced protoporphyrin-IX (PpIX) fluorescence guided surgery has been successful in macroscopic demarcation of tumor from healthy tissue.^{2,3} However, to match the level of resolution to that of histology, microscopic examination of brain structures is required. Confocal fluorescence imaging of ALA-induced PpIX^{4,5} and fluorescein⁶ have been reported to show promise in identifying neoplastic cells and distinguishing the tumor-brain interface. These methods are successful in

visualizing high-grade neoplasms; however, low-grade and infiltrating neoplasms often do not produce sufficient fluorescent signal.

In this paper, we present the first report on the feasibility of a dye-enhanced multimodal confocal approach for identifying brain neoplasms and distinguishing their subtypes, including high- and low-grade primary as well as metastatic brain cancers. Methylene blue (MB) was used to enhance contrast of the images. MB is a conventional histological stain, which is FDA approved for in vivo use. It has been successfully applied to grossly demarcate different types of cancer⁷⁻¹¹ and to track melanoma and breast cancer metastases in lymph nodes.^{12,13} It has also been shown to mimic the staining pattern of H&E in skin cancers.^{14,15} In general, reflectance imaging visualizes fluctuations of the refractive index of the tissue, whereas fluorescence imaging visualizes distribution and uptake of the MB. Therefore, combined reflectance and fluorescence imaging should provide complementary information on the optical and biochemical properties of the specimens. Fresh, thick, normal, and tumor tissues were collected, stained, and imaged. Acquired reflectance and fluorescence images of brain specimens were compared to corresponding H&E histopathology with the goal of identifying diagnostic features that could be useful for intraoperative delineation of brain neoplasms.

Address all correspondence to: Anna N. Yaroslavsky, University of Massachusetts, Department of Physics and Applied Physics, One University Avenue Lowell, Massachusetts 01854. Tel: 617 726 1590; Fax: 617 724 2075; E-mail: yaroslav@helix.mgh.harvard.edu.

2 Materials and Methods

2.1 Sample Handling

All experiments were conducted under the protocols approved by the institutional review boards of the Massachusetts General Hospital (MGH) and the University of Massachusetts at Lowell (UML). Normal and neoplastic brain specimens were gathered from resection surgeries performed at the Department of Neurosurgery at MGH, Boston, and sent to UML Advanced Biophotonics Laboratory for imaging.

Fresh samples were delivered to UML on ice within 1 to 12 hours of their acquisition from the operating room. The sizes of the specimens were between $2\text{ mm} \times 2\text{ mm} \times 2\text{ mm}$ and $40\text{ mm} \times 40\text{ mm} \times 40\text{ mm}$. Upon arrival to UML, the specimens were stained for 2 to 5 min, depending on the size of the specimen, in 0.05 mg/ml Phosphate Buffered Saline (Mediatech Inc. Manassas, VA) solution of MB (Methylene Blue Injection, 1%, American Regent Inc., Shirley, NY). The concentration of 0.05 mg/ml MB was empirically selected to provide optimal contrast of the confocal images. After staining, excessive dye was quickly rinsed off the samples. The samples were then moistened with saline solution (pH 7.4), covered with a microscopic cover slip, mounted in the sample holder [Fig. 1(a)], and imaged.

After imaging, the brain tissues were fixed in 10% formalin (Ricca Chemical Company, Arlington, TX) and processed for paraffin-embedded H&E histopathology.

2.2 Confocal Imaging

The schematic of the multimodal confocal system is presented in Fig. 1(b).^{14,15} A 642 nm diode laser (Micro Laser Systems,

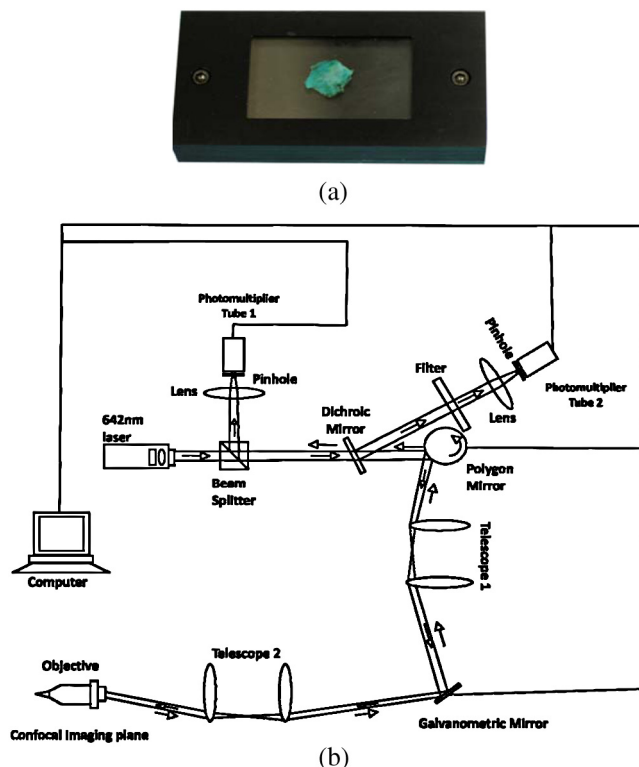


Fig. 1 (a) Image of brain tissue mounted in the sample holder. (b) Schematic diagram of the multimodal confocal system.

Garden Grove, CA) was used as the light source. The total power on the sample did not exceed 2.5 mW. Two photomultiplier tubes (PMT R9110 Hamamatsu, Bridgewater NJ) were employed for detection of reflectance and fluorescence signals. A polygon mirror (Lincoln Laser, Phoenix AZ) and galvanometric mirror (General Scanning Inc., Billerica MA) scanned the imaged point in the x and y directions, respectively. The scanning rate was set to 9 frames per second. The fluorescence signal was deflected by the 12-deg dichroic mirror (Iridian Spectral Technologies, Ottawa, Ontario) with a reflection band between 670 and 740 nm, and focused by a lens onto a 200- μm pinhole of the fluorescence PMT. To reject excitation light, a 690-nm bandpass filter with full width at half maximum of 40 nm (Chroma Technology Corp., Bellows Falls, VT) was installed in the fluorescence channel. A nonpolarizing beam splitter (CVI MellesGriot, Albuquerque, NM) and a lens were used to send elastically scattered signal into the 200- μm pinhole of the reflectance PMT. We employed two water immersion objective lenses, including $40\times/\text{NA}1.15$ and $60\times/\text{NA}1.2$ (Olympus, Melville, NJ), which provided a field of view of 370 and 250 μm , respectively. The system yielded lateral resolution better than 0.9 μm and axial resolution of 3 μm .

2.3 Histopathology

After imaging, tissue was formalin fixed and paraffin embedded in a plane corresponding to the plane of imaging to enable side-by-side correlation of optical images and histopathology. Sections 5 μm thick sections were cut and stained by standard H&E method.¹⁶ H&E sections were digitized using a Zeiss Axioskop microscope (Zeiss, Stuttgart, Germany) equipped with a $40\times$ objective lens, NA 1.0 (Zeiss) with the resolution of 0.36 μm . The resulting optical images were correlated with histopathology obtained from the same depth within the tissue.

3 Results and Discussion

In total, 91 tumor and 28 normal brain samples were imaged. Tumor samples included 52 gliomas [11 World Health Organization (WHO) Grade II, 13 WHO Grade III, and 28 WHO Grade IV], 14 meningiomas, and 25 metastases. Normal brain specimens were imaged for reference and comparison with the neoplastic tissue. These normal specimens were obtained from epilepsy surgeries, during which normal brain adjacent to the epileptogenic focus is routinely resected. They included white brain matter and gray brain matter. For all the specimens, reflectance and fluorescence images were acquired. Confocal images were compared side by side with corresponding histopathology. Results are presented in Figs. 2–8.

3.1 Normal Brain

Example images of white and gray brain matter are shown in Fig. 2. These images were taken from two different areas of a cross-section of the right temporal lobe. Comparison of white and gray matter images demonstrates clear differences in appearance, both in reflectance [Figs. 2(a) and 2(c)] and in fluorescence [Figs. 2(b) and 2(d)]. Reflectance images of both white and gray matter demonstrate lattice-like architecture of normal brain, with evenly spaced and well-organized processes. Myelin, a lipid with a high index of refraction that surrounds the axons in white matter, produces this dense, white,

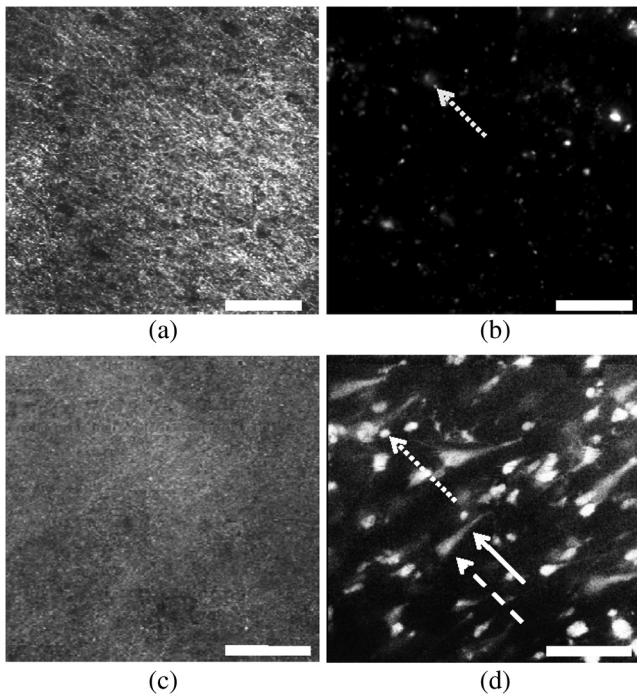


Fig. 2 Images of normal brain. Scale bar = 100 μm . (a) Reflectance image of white matter. (b) Fluorescence image of white matter. (c) Reflectance image of gray matter. (d) Fluorescence image of gray matter. Dotted arrows point to glial cells, dashed arrows point to neurons, and solid arrows point to axons.

mesh-like appearance. Due to the presence of the myelinated axons, the reflectance images of white matter [Fig. 2(a)] are brighter, as compared with gray matter [Fig. 2(c)]. The fluorescence image of normal gray matter [Fig. 2(d)] presents neuronal cell bodies (dashed arrow), which in our images were approximately 27 μm in size with exiting nonmyelinated axons (solid arrow) that stretch about 52 μm . Glial cells, shown with dotted arrow, are also present and are approximately 9 μm in size. Normal white matter tissue is made up of glial cells and myelinated axons.¹⁷ Glial cells can be detected by the fluorescence imaging [Fig. 2(b), dotted arrow], but the dielectric properties of myelin surrounding the axons in white matter prevent uptake of MB, and as a result axons are not apparent in the fluorescence

image of white matter. These results are in good correlation with previously reported observations.¹⁷

3.2 Meningiomas

Meningiomas arise from the arachnoid layer of the meninges, the membranes that surround the brain and the spinal cord. They most commonly present with seizures; focal neurological deficits, if the tumor is near regions of the brain such as the motor or language cortex; or signs and symptoms of elevated intracranial pressure.^{18,19} These tumors take the shape of the area they occupy, forming circles around one another.¹⁹ Figure 3 shows typical meningothelial whorls that can be seen in both reflectance [Fig. 3(a)] and fluorescence [Fig. 3(b)] confocal images. In the reflectance image, the fibrous outer layer of the meningial whorls (dashed arrows) can be clearly distinguished. Interestingly, meningiomas do not exhibit the dense lattice like structure of the normal brain tissue [Figs. 2(a) and 2(c)]. In contrast to reflectance, the fluorescence image [Fig. 3(b)] demonstrates cellular inner parts of the whorls (solid arrows). It should also be noted that the combination of reflectance and fluorescence images provides complementary information about the structure of meningiomas. Comparison with respective H&E histopathology demonstrates good correlation with both reflectance and fluorescence images.

3.3 Glial Neoplasms

Gliomas are the most common and deadly type of intrinsic brain tumors.²⁰ They originate from the macroglial cells. The glial cells provide nutrients and oxygen to the neurons, electrochemically insulate them from one another, destroy pathogens, and remove debris. Three types of glial cells, including astrocytes, oligodendrocytes, and ependymal cells, can give rise to glioma. Astrocytes serve to regulate blood flow and chemical balance of neurons in the brain and are the most abundant of the macroglial cells. Oligodendrocytes form the myelin sheath that insulates the central nervous system axons. Ependymal cells create and regulate the flow of cerebrospinal fluid.²¹ According to their biological behavior, gliomas are graded in four categories by the WHO. Grade I tumors are typically well encapsulated and may be cured with a complete resection. Grades II through IV are typically diffuse and infiltrative, and recur as a rule. Associated survival times shorten with increasing grade. Grade II tumors are also known as low-grade gliomas

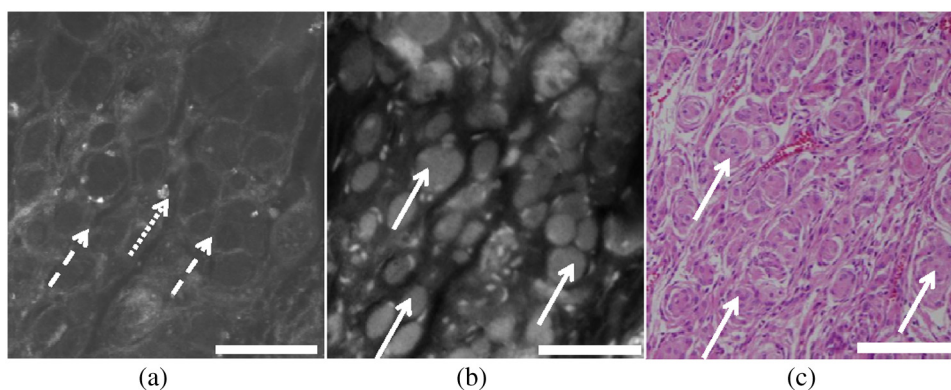


Fig. 3 Images of meningioma. Scale bar = 100 μm . (a) Reflectance image. (b) Fluorescence image. (c) H&E histopathology. Dashed arrows point toward fibrous outer layer of meningial whorls seen in the reflectance image. Dotted arrows point toward calcifications. Solid arrows point toward cellular inner part of meningial whorls seen in fluorescence and histopathology.

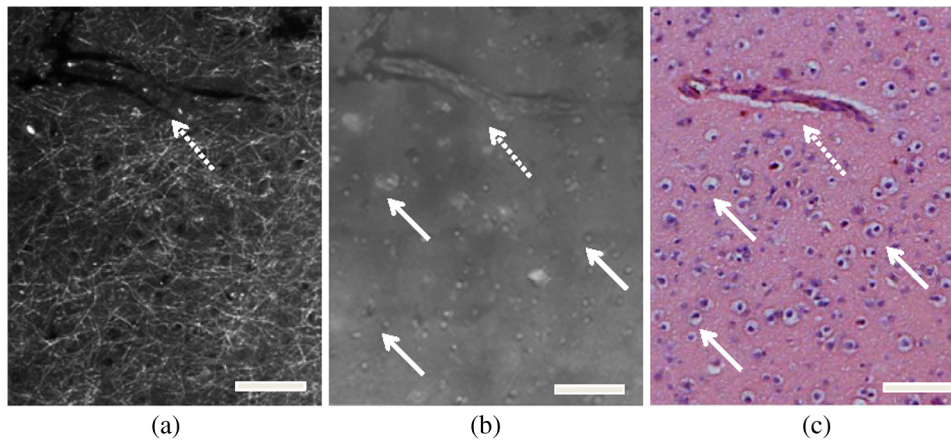


Fig. 4 Images of low-grade astrocytoma. Scale bar = 100 μm . (a) Reflectance image. (b) Fluorescence image. (c) H&E histopathology. In fluorescence and histology images, glioma cells are shown with solid arrows. Dotted arrows point toward a blood vessel in reflectance, fluorescence, and histology images.

(LGG). Grade III (anaplastic) and IV (glioblastoma) are high-grade tumors.²² Optical images were registered for all of the above-mentioned glioma grades.

3.3.1 Low-Grade Gliomas

LGGs can be divided into two main groups: pilocyticastrocytomas, WHO Grade I, which have distinctive histological features, and WHO Grade II gliomas, which include diffuse astrocytoma, oligodendroglioma, and oligoastrocytoma. Diffuse astrocytomas are the most difficult to distinguish from normal brain tissue due to a low number of tumor cells; often-minimal nuclear pleomorphism; and absence of mitotic figures, necrosis, and microvascular proliferation. Diffuse astrocytomas often show only a

mild to moderate increase of cellularity with nuclear atypia and are notoriously challenging to diagnose on frozen sections.

Figure 4 shows images of LGG, WHO Grade II astrocytoma. Reflectance image [Fig. 4(a)], reveals a structure that differs from that found in reflectance images of normal brain matter [Figs. 2(a) and 2(c)]. In the fluorescence image [Fig. 4(b)], which correlates well with the histology image [Fig. 4(c)], there is a slightly increased density of glial cells (solid arrows) as compared with the fluorescence image of normal white brain matter [Fig. 2(b)]. Slightly increased cellularity is a common characteristic of LGG. In Figs. 4(a)–4(c), a blood vessel can be seen (dotted arrow). Figure 5 shows higher-magnification images of the specimen presented in Fig. 4. In low-grade gliomas, tumor cells tend to cluster around neurons. This phenomenon is known as satellitosis. In fluorescence [Figs. 5(b) and 5(e)] as well

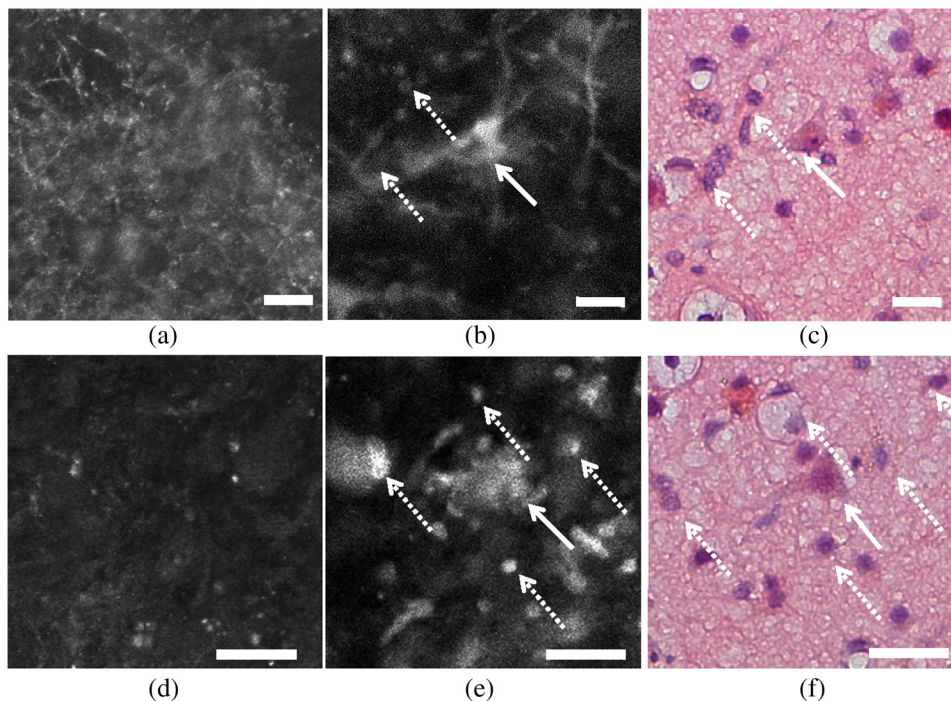


Fig. 5 High-magnification images of low-grade astrocytoma. Scale bar = 25 μm . (a) and (d) Reflectance image. (b) and (e) Fluorescence image. (c) and (f) H&E histopathology. In the fluorescence and histology images, solid arrows point to a neuron. Dotted arrows point toward glioma cells that surround the neuron.

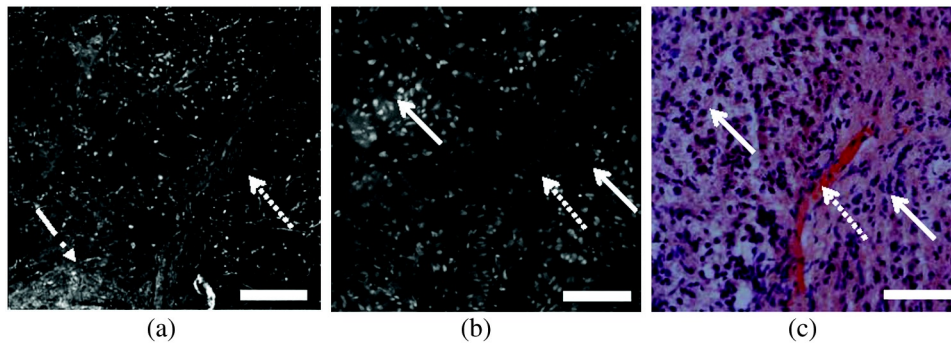


Fig. 6 Images of high-grade astrocytoma. Scale bar = 100 μm . (a) Reflectance image. (b) Fluorescence image. (c) H&E histopathology. Solid arrows point toward glial cancer cells. Dotted arrows point toward a blood vessel. Dashed and dotted arrow points toward the clumped processes.

as in histology images [Figs. 5(c) and 5(f)], a neuron can be seen (solid arrow) with glioma cells (dotted arrows) crowded around it. The reflectance image [Figs. 5(a) and 5(d)] of LGG presents disruption of the normal brain architecture, revealed in Figs. 2(a) and 2(c). In the case of LGG, the fluorescence images [Fig. 4(b)] appear to be a good indicator of abnormally increased cellularity, which upon high-power inspection of reflectance [Fig. 5(a)] and fluorescence images [Fig. 5(b)], reveals loss of normal brain architecture and satellitosis, respectively.

3.3.2 High-Grade Gliomas

High-grade gliomas (HGGs) can be divided into WHO Grade III and WHO Grade IV tumors. WHO Grade III neoplasms are anaplastic tumors, including astrocytoma, oligodendroglioma, and oligoastrocytoma. They are characterized by increased cellularity, nuclear pleomorphism, and atypia. Compared with normal brain, cell density is significantly increased. Example images of high-grade glioma, WHO Grade III anaplastic astrocytoma, are presented in Fig. 6. Reflectance image of HGG, presented in Fig. 6(a), is dramatically different from those of normal brain [Figs. 2(a) and 2(c)]. Normal brain architecture is lost due to abundant cancer cells, which are revealed in fluorescence image presented in Fig. 6(b) and shown with a dash and dotted arrow. These cancer cells obliterate and destroy normal brain architecture, as can be seen in Figs. 6(a) and 6(b). The pattern of fluorescence image [Fig. 6(b)] correlates well with that of histopathology [Fig. 6(c)].

WHO Grade IV cancers, glioblastomas (GBMs), are the most malignant of glial tumors. In addition to the signs of Grade III neoplasms, glioblastoma is characterized by microvascular proliferation and necrosis.²³ Figure 7 shows a sample of

GBM. Reflectance [Fig. 7(a)] and fluorescence [Fig. 7(b)] images are presented sidebyside with corresponding H&E histopathology [Fig. 7(c)]. The fluorescence and histopathology images demonstrate that the density of cancer cells in GBM is even higher than in Grade III neoplasm, presented in Fig. 6. The vascular proliferations (dashed arrows) and multiple crowded glioma cells (solid arrows) surrounding the vessels are distinctly visible in the fluorescence images [Fig. 7(b)]. Overall morphology of the sample outlined in the fluorescence image compares well with histopathology [Fig. 7(c)]. Rapid cell proliferation, abnormal angiogenesis, and hypoxia lead to development of areas of necrosis. These necrotic areas are characterized by the loss of signal in both reflectances [Fig. 7(a)] and fluorescence [Fig. 7(b)] images. They are shown with dotted arrows in the optical and histopathology images [Fig. 7(c)].

3.4 Metastases

Metastatic brain tumors account for about one-fourth of all cancers that metastasize. They are much more common than primary brain malignancies and occur in approximately 10% to 30% of adult cancers. These tumors often retain morphological features of their primary cancer, and their appearance is remarkably different from that of normal brain, meningioma, or any of the glial neoplasms. Out of cancers that metastasize to the brain, the most common are lung, breast, renal carcinomas, and melanomas.²⁴ Example reflectance, fluorescence, and histological images of a metastatic lung adenocarcinoma are presented in Figs. 8(a), 8(b), and 8(c), respectively. As expected, clear differences can be revealed between the metastatic tumor and all the primary brain neoplasms imaged. In all the images, carcinoma nodules are shown with solid arrows. They are

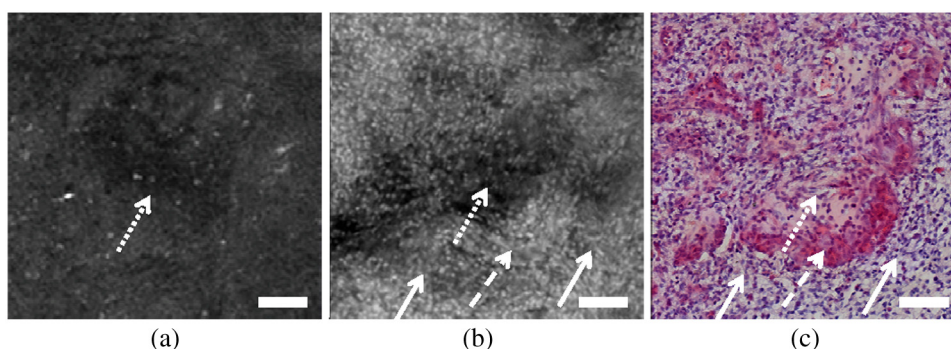


Fig. 7 Images of glioblastoma. Scale bar = 100 μm . (a) Reflectance image. (b) Fluorescence image. (c) H&E histopathology. Solid arrow points toward clumped masses of glial cells. Dotted arrows point toward necrosis. Dashed arrows point toward vascular proliferations.

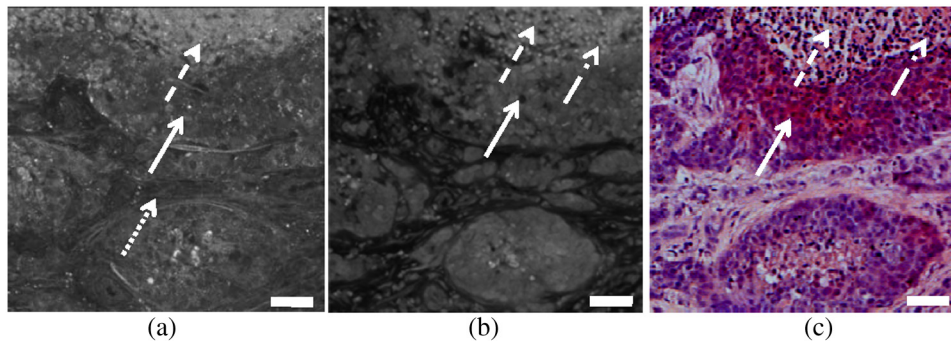


Fig. 8 Images of metastatic lung carcinoma. Scale bar = 100 μm . (a) Reflectance image. (b) Fluorescence image. (c) H&E histopathology. Solid arrows point toward carcinoma nodules. Dotted arrows point toward dense bands of fibrous tissue. Dashed arrows point toward necrosis. Dashed and dotted arrows point toward macrophages in the necrotic area.

surrounded by dense bands of fibrous tissue shown with dotted arrow, whereas dashed arrows point to necrotic tissue. Dash and dotted arrows point toward the macrophages that can be seen in fluorescence images and in corresponding histopathology. Similarly to the other tumors, reflectance [Fig. 8(a)] and fluorescence [Fig. 8(b)] combine to provide essential information on the morphology and architecture of the specimen. Both optical images correlate well with respective H&E histopathology and enable clear differentiation among viable carcinoma, necrosis, and mesenchymal tissue.

4 Summary and Conclusions

The results of our study demonstrate that simultaneous reflectance and fluorescence confocal imaging of freshly excised thick normal and neoplastic brain tissue, topically stained with aqueous solution of an FDA-approved contrast agent, MB, can be successfully used for high-resolution inspection of brain structures. We presented high-quality images of brain tissue morphology, which allowed neuropathologists to recognize typical histological patterns when compared with traditional histology. Reflectance and fluorescence images provide distinctly different and complementary information on brain tissue morphology. For example, fluorescence images of normal brain and glioma visualize different types of cells, including neurons and glial cells, vascular proliferations, and necrosis. Appearance of brain cells and structures is similar to that in histopathology. In contrast, reflectance images show cell processes. These images present structures that are not visualized by H&E histopathology. Comparison of reflectance images of normal white brain matter and gliomas demonstrate a transition from the well-ordered lattice like appearance of normal tissue [Fig. 2(a)], through a partially disrupted yet still structured background in low-grade gliomas [Figs. 4(a) and 5(a)], to the disorganized pattern with clumped processes in anaplastic gliomas [Fig. 6(a)], and complete loss of structure and partial loss of signal in glioblastomas [Fig. 7(a)]. Analysis of these changes in reflectance images may yield an additional parameter for evaluation of brain involvement with cancer and/or for staging the disease. In the case of meningiomas (Fig. 3) and metastatic cancers (Fig. 8), both reflectance and fluorescence images demonstrate good correlation with respective histopathology. In contrast to normal brain tissue and glial neoplasms, reflectance images of these tumors do not exhibit any processes of brain tissue.

We found that for all the tissue types investigated, fluorescence images correlated well with corresponding H&E

histopathology. The magnification and resolution of the optical images is adequate for the inspection of single cells. Diagnostic features in fluorescence images appear similar to those in histopathology. This should simplify image interpretation by pathologists and help with translation of this technology to clinical practice. Our findings suggest that combined reflectance and fluorescence confocal examination of brain tissue shows promise for the intraoperative diagnosis of brain neoplasms and possibly also for evaluation of resection margins. However, to be practical for intraoperative demarcation of abnormal tissue during surgery, the technology should enable quick inspection of large brain areas in addition to high-resolution examination of the cellular detail and organization. Therefore, our future work will focus on implementing and validating wide-field and high-resolution imaging in a single device.

Acknowledgments

We gratefully acknowledge Irina Tabatadze for processing histopathology and Polina Ogas for help with sample transportation. Funding was provided by the Massachusetts General Hospital Cancer Center and a seed grant from the University of Massachusetts at Lowell.

References

1. N. Sanai and M. S. Berger, "Glioma extent of resection and its impact on patient outcome," *Neurosurgery* **62**(4), 753–766 (2008).
2. W. J. Whitson et al., "Confocal microscopy for the histologic fluorescence pattern of a recurrent atypical meningioma; case study," *Neurosurgery* **68**(6), 753–766 (2011).
3. W. Stummer et al., "Fluorescence-guided resection of glioblastoma multiforme by using 5-aminolevulinic acid-induced porphyrins: a prospective study in 52 consecutive patients," *J. Neurosurg.* **93**(6), 1003–1013 (2000).
4. W. J. Whitson et al., "Confocal microscopy for the histologic fluorescence pattern of a recurrent atypical meningioma," *Neurosurgery* **62**(4), 753–766 (2011).
5. T. C. Ryken et al., "Surgical management of newly diagnosed glioblastoma in adults: role of cytoreductive surgery," *J. Neuro-Oncol.* **89**(3), 271–283 (2001).
6. N. Sanai et al., "Intraoperative confocal microscopy for brain tumors: a feasibility analysis in humans," *Neurosurgery* **68**(2), 282–290 (2011).
7. W. B. Gill et al., "Selective surface staining of bladder tumors by intravesical methylene blue with enhanced endoscopic identification," *Cancer* **53**(12), 2724–2727 (1984).
8. A. V. Kaisary, "Assessment of radiotherapy in invasive bladder carcinoma using in vivo methylene blue staining technique," *Urology* **28**(2), 100–102 (1986).

9. I. Fukui et al., "In vivo staining test with methylene blue for bladder cancer," *J. Urol.* **130**(2), 252–255 (1983).
10. U. Fedorak et al., "Localization of islet cell tumors of the pancreas: a review of current techniques," *Surgery* **113**(3), 242–249 (1983).
11. A. N. Yaroslavsky, V. Neel, and R. R. Anderson, "Demarcation of nonmelanoma skin cancer margins using multispectral polarized-light imaging," *J. Invest. Dermatol.* **121**(2), 259–266 (2003).
12. E. M. Link and R. N. Carpenter, "²¹¹At-Methylene blue for targeted radiotherapy of human melanoma xenografts: treatment of cutaneous tumors and lymph node metastases," *Cancer Res.* **52**(16), 4385–4390 (1992).
13. P. Varghese et al., "Methylene blue dye—safe and effective alternative for sentinel lymph node localization," *Breast J.* **14**(1), 61–67 (2008).
14. M. Al-Arashi, E. Salomatina, and A. N. Yaroslavsky, "Multimodal confocal microscopy for the detection of nonmelanoma skin cancers," *Las. Surg. Med.* **39**(9), 706–715 (2007).
15. J. Park et al., "Dye-enhanced multimodal confocal microscopy for non-invasive detection of skin cancers in mouse models," *J. Biomed. Opt.* **15**(2), 026023 (2010).
16. "Paraffin Section Method and Technique," IHC World, Retrieved 11, August, 2011, from http://www.ihcworld.com/_protocols/histology/paraffin_section.htm.
17. P. G. Bhatia and E. M. L. Sklar, "Neuroimaging: structural neuroimaging," Chapter 36 A in *Neurology in Clinical Practice*, 5th ed. W. G. Bradley, R. B. Daroff, G. M. Fenichel, and J. Jankovic, Eds. (Butterworth-Heinemann Elsevier, Philadelphia, PA, 2008).
18. P. Black et al., "Meningiomas: science and surgery," *Clin. Neurosurg.* **54**, 91–99 (2007).
19. D. Monleón et al., "Metabolic aggressiveness in benign meningiomas with chromosomal instabilities," *Cancer Res.* **70**(21), 8426–8434 (2010).
20. R. A. Prayson, "Histological classification of high-grade gliomas," Chapter 1, in *High-Grade Gliomas: Diagnosis and Treatment*, G. H. Barnett, ed. (Humana Press Inc., Totowa, NJ, 2007).
21. P. R. Laming and E. Syková, *Glial Cells: Their Role in Behaviour*, pp. 4–9 (Cambridge University Press, New York, 1998).
22. "Brain tumor classification, grading, and epidemiology," Chapter 1, in *Brain Tumors*, H. Greenberg, W. F. Chandler, and H. M. Sandler, Eds., pp. 17–18 (Oxford University Press, New York, 1999).
23. A. Drevelegas, "High grade gliomas," Chapter 6, in *Imaging of Brain Tumors with Histological Correlations*, 2nd ed., A. Drevelegas and G. Karkavelas, Eds., p. 159 (Springer, New York, 2011).
24. J. Sul and J. B. Posner, "Brain Metastases: Epidemiology and Pathophysiology," Chapter 1, in *Brain Metastases*, J. J. Raizer and L. E. Abrey, Eds. (Springer, New York, 2007), pp. 1–4.